CERN Summer Student Programme

A comprehensive study of the characteristics of a single bar from the proposed ToF detector

Author:
Irene Andreou

Supervisors:
Prof. Federico Sanchez
Stefania Bordoni

September 10, 2021

Abstract

Neutrino Physics has the potential to revolutionise our understanding of how the universe works. Measurements of neutrinos coming from the Sun or produced by cosmic rays in the Earth's atmosphere shed light on neutrino oscillations, leading to groundbreaking information on neutrino masses and their mixing [1]. One experiment studying neutrino oscillations is the T2K (Tokai to Kamioka) experiment in Japan. Commissioned in 2009, it will now be upgraded to increase its sensitivity [2]. A part of the upgrade involves the introduction of a Time-of-Flight (ToF) detector surrounded by a new fine-grained fully-active plastic scintillator detector(Super-FGD) and two high angle Time-Projection Chambers (TPCs)[2]. In this paper, we investigate the single-bar cosmic ray data from the proposed ToF detector, characterise light propagation in the bar, and describe arrival time distribution and time resolutions. A model on light propagation and intensity evolution through the bar is proposed and tested and the time resolution as a function of location along the bar is portrayed.

Acknowledgements

The author would like to express her most profound gratitude towards Professor Federico Sanchez and Stefania Bordoni for their guidance and support over the past thirteen weeks. Their invaluable assistance in performing the analysis of single-bar data from the ToF detector has made this project an incredible and eye-opening experience. Furthermore, even though the nature of the work was remote, the author has never felt more connected and encouraged to be part of the Neutrino Physics group at the University of Geneva. Furthermore, the author expresses her thanks to the Summer Student Team at CERN for creating these opportunities for undergraduate students and Dr Brindley and Professor Golutvin for aiding her in the application process. Lastly, the author extends her deepest gratitude to Mrs.Tasoula Andreou and Mrs.Maroulla Mappoura for their moral support and encouraging words throughout this summer period.

Contents

Chapter 1

Introduction

1.1 The T2K experiment

T2K (Tokai to Kamioka) is a long-baseline experiment located in Japan studying neutrino oscillations. *Neutrino Oscillations* is a quantum mechanical phenomenon that takes place because flavour neutrinos (electron, muon, tau neutrinos) are superpositions of mass states [1]. If neutrinos are massive and each flavour's mass is different, they will propagate in varied ways. Therefore, as time evolves, their combination can correspond to a different type of neutrino, leading to neutrino oscillations. The T2K experiment propagates an intense muon neutrino beam from Tokai (east coast of Japan) to Kamioka (western Japan) [2]. The beam is generated in collisions between a proton beam and a graphite target, producing pions and kaons that are then focused by magnetic devices [2]. The pions are short-lived and thus quickly decay to muons and muon neutrinos. The remaining protons, pions, and muons are hindered via the second layer of graphite while the neutrinos pass straight through and constitute the aforementioned beam [2]. The beam of neutrinos is measured at the near detector, located 280 m away from the target and observed after oscillation at the Super Kamiokande detector, located 250 km away from the target and 1000 m underground [2].

1.2 The ND280 near detector and its upgrade

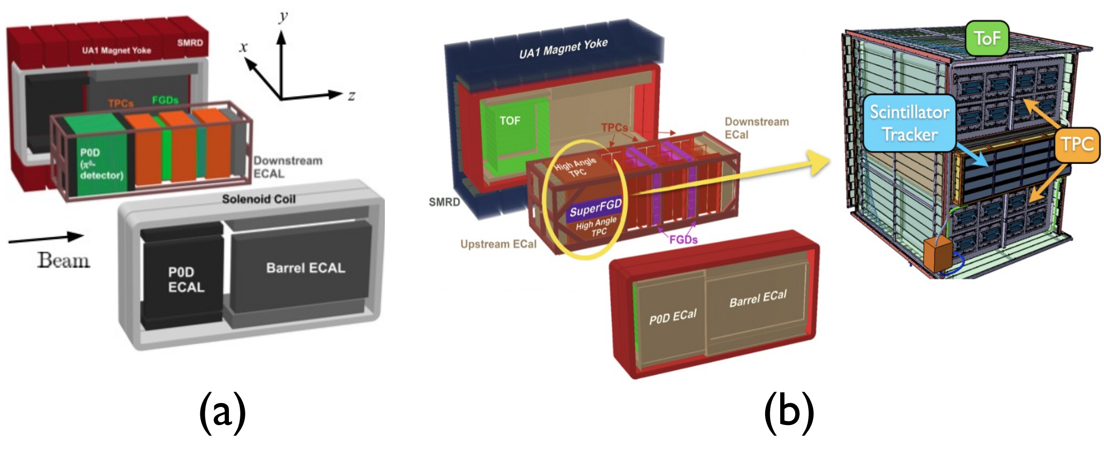

Figure 1.1: Schematics of the old ND280 near detector configuration in (a) and the new configuration in (b). Adapted from [1,3].

The T2K experiment has been commissioned since 2009 and is now due for an upgrade. Part of the process involves the upgrade of the ND280 near detector. The ND280 detector upgrade consists of the replacement of the π_0 detector (P0D) with a Time-of-Flight (ToF) detector surrounding a new fine-grained fully-active plastic scintillator detector (Super-FGD) which improves angular acceptance and two high angle Time-Projection Chambers (TPCs) [1]. The old configuration of the ND280 detector, illustrated in fig. 1.1(a), consisted of a UA1 magnet tasked with measuring the momenta of the particles produced in the near detector, a P0D optimised for measuring the production rate of neutral current π^0, a tracker made of three TPCs and two FGDs used to characterise the background and momentum of particles produced in charged current interaction [4]. Surrounding the detector core is an electromagnetic calorimeter (ECAL) which distinguishes between the signature of single electrons and photons [4]. In the old configuration, the first TPC was tasked with identifying background interactions coming from outside the detector and removing them from the signal. The following consecutive FGDs and TPCs represent where most of the neutrino interactions were characterised [4]. The event tracks leave the FGDs and enter the TPC, filled with a gaseous medium, in which the curvature of the track is prominent due to the presence of a magnetic field. Using the curvature, the momentum and particle type can be inferred. Schematics of the old and new configurations are depicted in fig. 1.1.

The upgrade will improve the rejection of the background due to interactions coming from outside the target, which is a source of systematic error for the current analysis [1]. The ToF detector consists of six planes. Each plane is assembled with twenty 2.2 m long plastic scintillator bars (EJ-200 [5]). Each bar has silicon photomultipliers arrays on both ends, which collect the light. Over the past thirteen weeks, the author has worked on characterising the performance of the ToF detector using single-bar data obtained during a period of data taking.

Chapter 2

ToF Single-Bar Data

The purpose of the single-bar data is to assess the performance of the ToF detector. Using the single-bar data presents the opportunity to expose possible intrinsic signal delays, characterise the detector's time resolution and examine the behaviour of the propagation velocity in a single bar.

2.1 Signal Clean-up and Visualisation

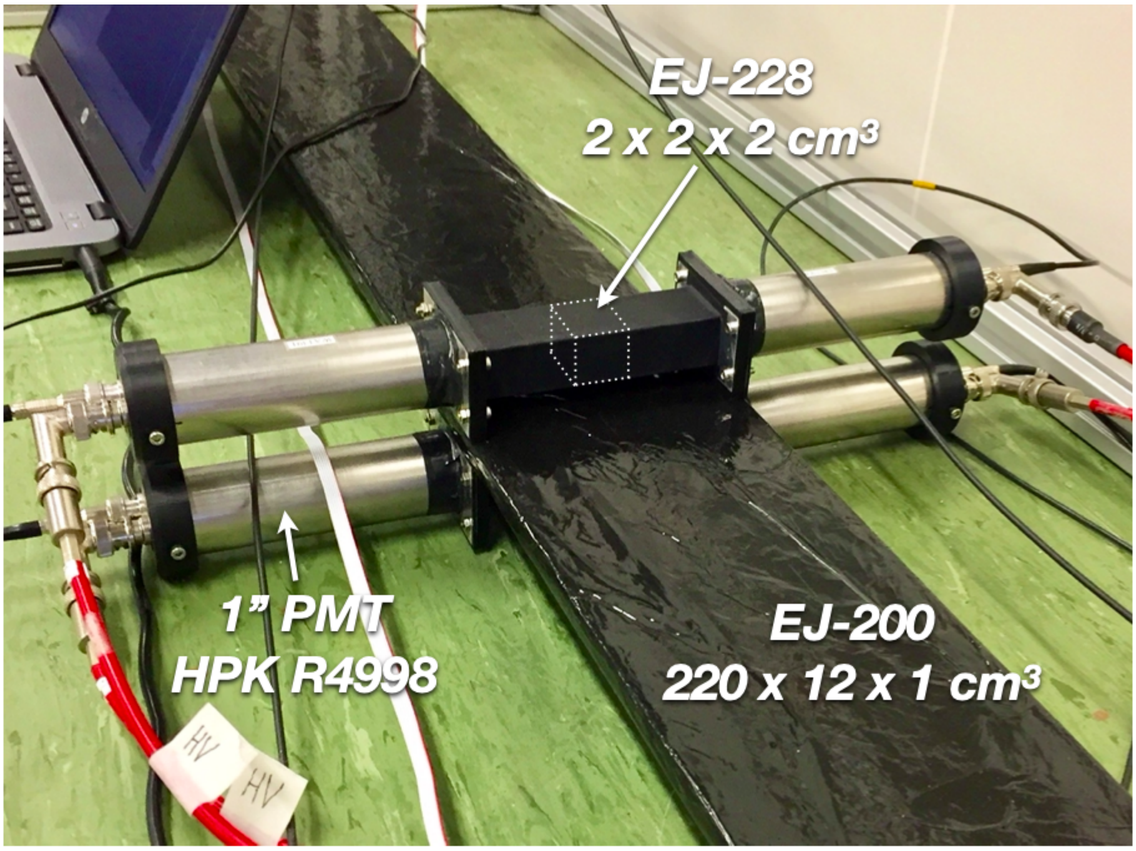

Figure 2.1: Setup used for single-bar data collection. Produced by Dr Alexander Korzenev.

The setup used to collect the single-bar data is shown in fig. 2.1. The setup included a bar mounted with the SiPM arrays as foreseen in the final ToF module and the use of an external trigger made of two cubes (2 x 2 x 2 cm^3) positioned on the top and bottom of the bar. Each of the cubes is read by two vacuum photomultiplier tubes (PMTs). This external trigger can slide along the bar allowing for measurements to be taken at different locations along the bar (5 cm, 10 cm, 20 cm, 50 cm, 80 cm, 110 cm, 140 cm, 170 cm, 200 cm, 210 cm, 215 cm). The data collected was from cosmic rays. An event was identified via simultaneously recording a signal on the two identical cubes located at the top and bottom of the bar. The trigger time of each event was calculated as the average time recorded by the four PMTs. For each event, 1024 points were produced from each of the two silicon photomultipliers (SiPMs) at the bar ends, at a sampling frequency of 3.2 GHz, giving sufficient information for the reconstruction of each waveform.

Visualising the events recorded at each location led to the conclusion that selection cuts needed to be applied in order to remove noise incurred from the electronics, saturated and double signals. The clean-up was performed in steps. First, a saturation cut was applied whereby signals such

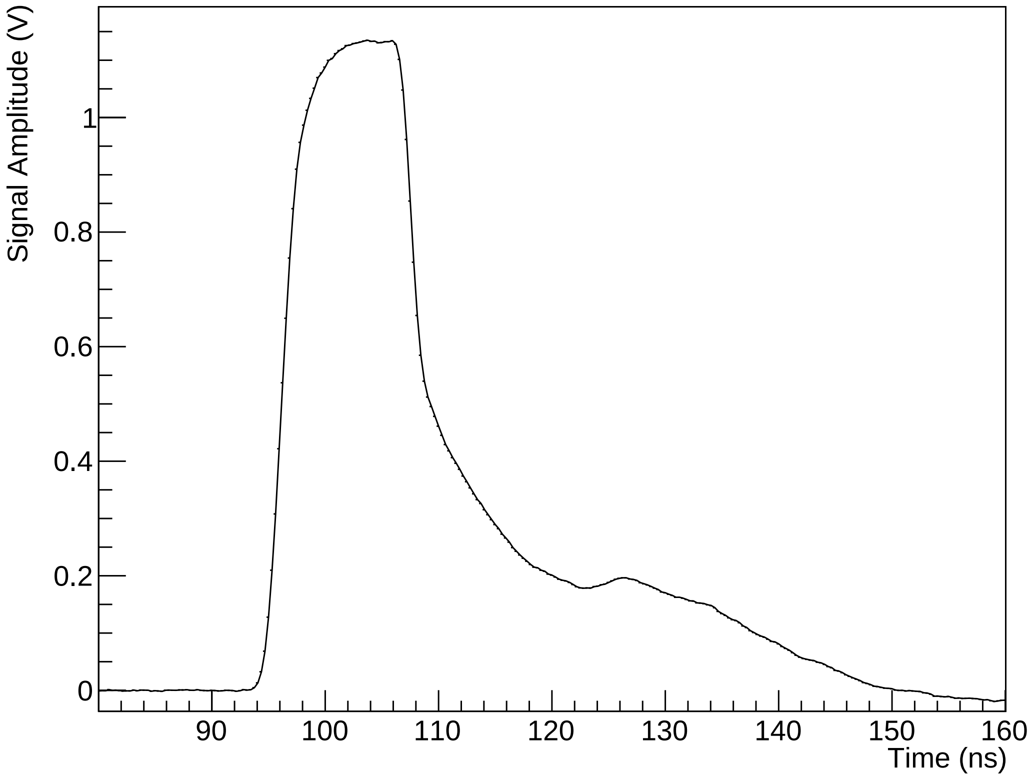

Figure 2.2: An example of a saturated signal.

as the one shown in fig. 2.2 below were removed. In order to identify the saturated signals, each signal was filtered through an algorithm comparing its maximum amplitude to the amplitudes of the neighbouring time ticks. If the signals exhibited a plateau (Δ amplitude <0.005 V), they were rejected. To ensure that all saturated signals were removed, an additional clause was added to the saturation cut, removing all signals with a maximum amplitude greater than 1.05 V.

The saturation cut was followed by a selection cut on the trigger amplitudes. This was motivated by fig. 2.3, which shows the PMT amplitude distributions of all the recorded events from one of the two SiPMs after the saturation cut was applied. As can be seen from fig. 2.3, the signal amplitude distribution of each PMT is comprised of a decreasing exponential which corresponds to the background noise and a peak that indicates a cosmic muon passing through the bar. Instead of applying a conservative cut on each individual trigger amplitude, the author studied the amplitude correlations to develop a systematic methodology for the trigger amplitude cut. The amplitudes recorded by the PMTs will be highly correlated because each pair of PMTs on either side of the bar reads the same cube. Thus, when a cosmic muon passes through the two cubes, we expect all four PMTs to record something almost simultaneously. Identifying those pairs as 0-1 (top of the

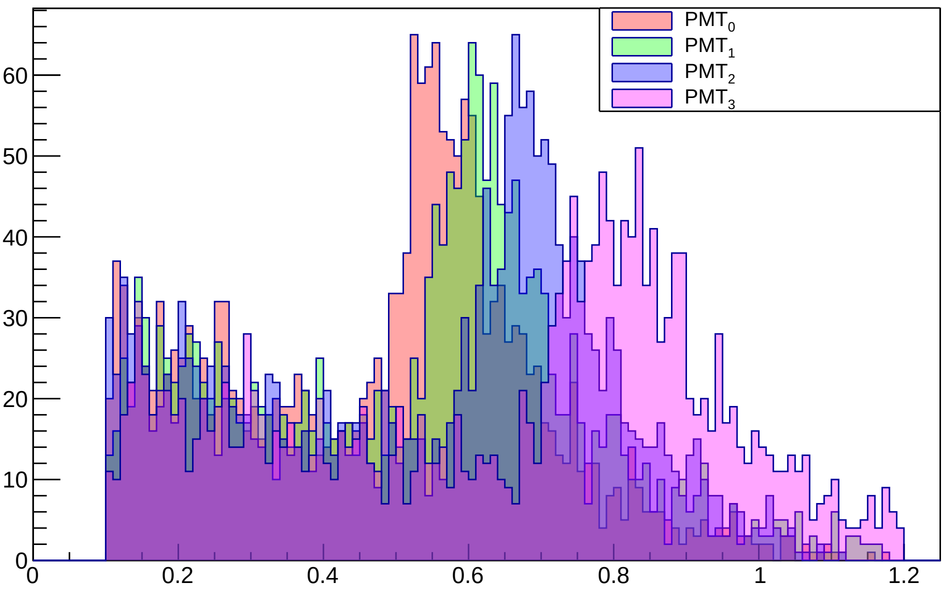

Figure 2.3: Trigger Amplitude signal recorded by the four PMTs. There is a clear distinction between the exponential background and the signal peak.

bar) and 2-3 (bottom of the bar), fig. 2.4 was produced. From the two figures, there is a prominent high correlation region around 0.6-0.8 V, but there are also some apparent high correlation events at 0.1 V, which can be classified as noise based on fig. 2.3. The subplots in fig. 2.4 are combined in a single correlation plot in fig. 2.5 in order to study the correlation between the two pairs of PMTs. The axes of fig. 2.5 represent the sum of the two signal amplitudes recorded by the PMTs on top (x-axis) and the bottom (y-axis) of the bar. Events that show a high correlation in fig. 2.5 signify cosmic muons that pass straight through both cubes surrounding the bar, whereas lower amplitude correlations in fig. 2.4 correspond to cosmic muons partially passing through the detector. Based on the amplitude sum correlation plots, the trigger cut amplitudes are set at 1.0 (x-axis) and 1.25 (y-axis).

Lastly, a selection cut based on the integral/maximum distribution was performed. The integral represents the area of the signal in the region between 90 and 140 ns, and the maximum indicates the peak value of each signal. The motivation behind this particular selection cut was to remove the remaining double or noise signal events with a random integral/maximum ratio. It is expected that if a signal is well-behaved, then the ratio integral/maximum will be narrow. Based on the above, fig. 2.6 was produced. As can be observed from fig. 2.6, there appear a few sparse deviations from the overall shape of the distribution with integral values much greater than anticipated. Studying the signal distributions in small integral value intervals led to the construction of Gaussian distributions with elongated tails, which were removed with a cut on:
fluctuations $> 2\ \sigma$.

In this part of the investigation, a conclusion that the geometry of the external trigger inhibits any further improvement on the signal selection was reached. What has been attempted above is the selection of good PMT signals crossing the two scintillators, where very good PMT signals indicate signals that have fully crossed the detector. Such good signals are almost definitely in sync or slightly shifted with respect to each other.

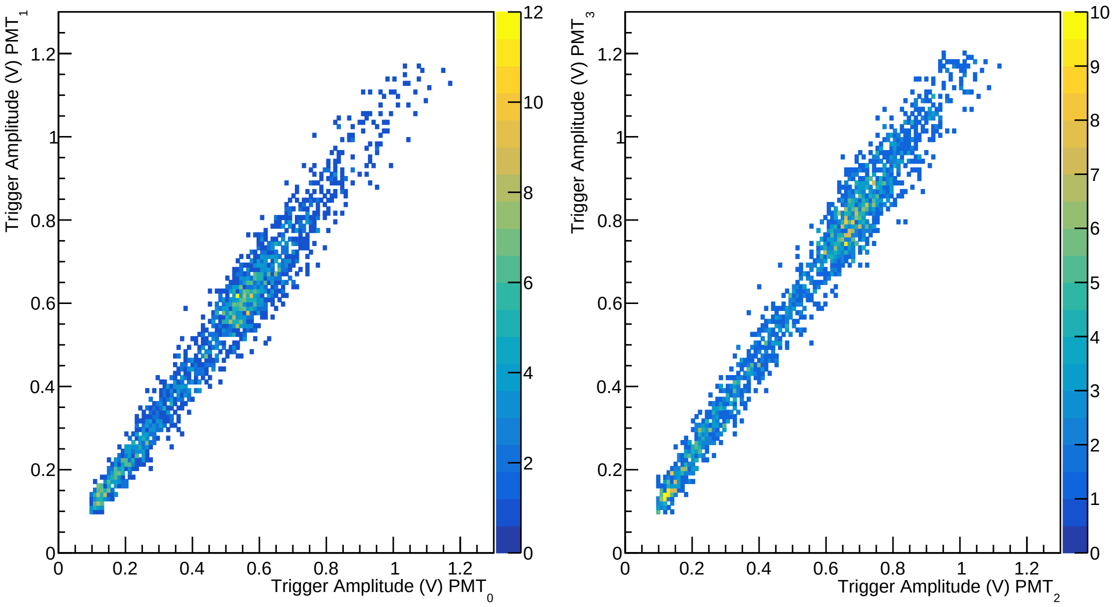

Figure 2.4: Trigger amplitude correlation plots for the pairs 0-1 (left) and 2-3 (right).

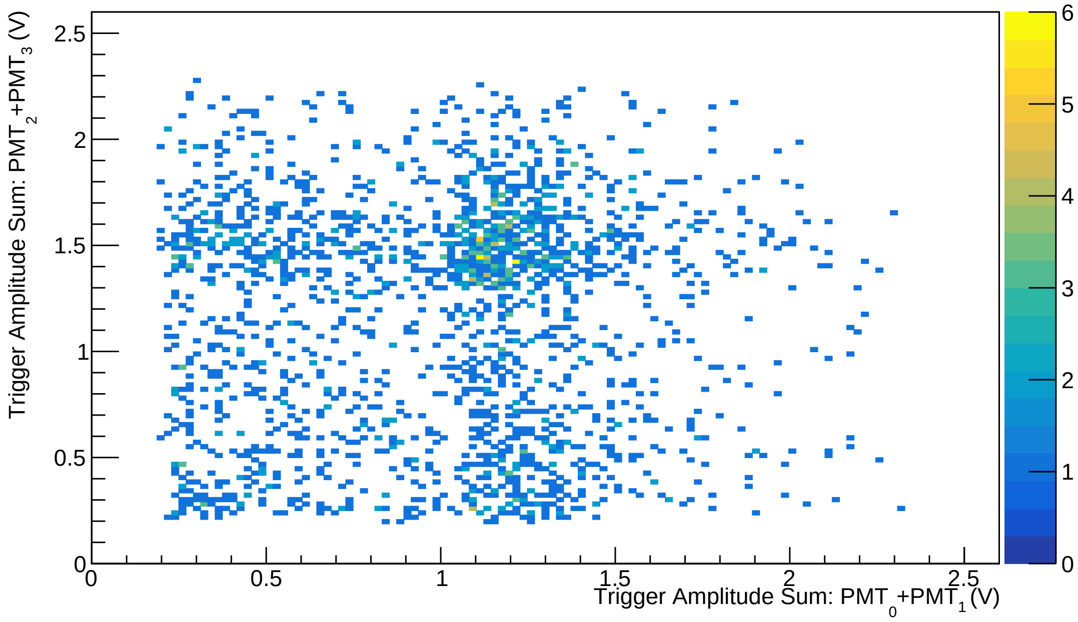

Figure 2.5: Sum of trigger amplitude pairs correlation plot.

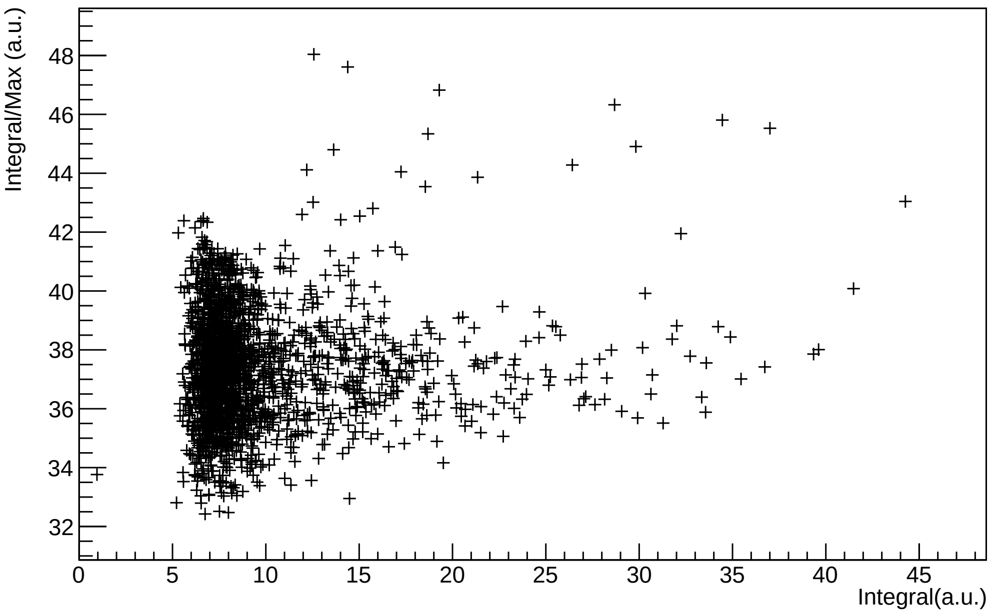

Figure 2.6: Example integral/maximu distribution before applying the final cut.

2.2 Detector Behaviour Characterisation

Once the selection process was concluded, the pedestal was removed. Then the averaged waveform at each location was produced. All average amplitudes were compiled on the same plot to examine the detector's response with regard to signals passing through different locations. The pedestal was calculated as the average value of the first 50 points of each accepted signal and then subtracted from the signal before averaging. Before averaging the signals, they were normalised with respect to their respective integral values. An example averaged signal with the RMS errors is shown in fig. 2.7, where time-shifting was also applied to remove the remnant effects of the orientation of the cosmic muon when it crosses the bar and any random signal reflection paths. Fig. 2.7 shows with no ambiguity that this is indeed a signal. The errors are more significant when the slope is larger and around the second bump, which is expected. The second bump is caused by reflected signals that have a statistical nature, which justifies the fluctuation from event to event.

When plotting all averaged signals on the same graph, the errors were not shown to ensure clarity of the plot. In fig. 2.8 the averaged signals from both sensors are shown. An overall trend is exhibited whereby the signal amplitude decreases from the 5 cm to the 170 cm location respectively for each sensor. This can be explained by the fact that light propagates through the bar in 4π, so at any location, there are two components to the signal: **"direct"** and **"reflected"**, where the reflected signal is caused by the propagation of light throughout the bar, being reflected and returning. As expected, the direct signal contribution forms a prompt narrow signal, whereas the reflected contribution populates a delayed signal. Summing the two gives the total amplitude of the waveform at any time. The shorter the distance between the front end of the bar and the trigger, the more prompt and narrow the overall signal is as it is dominated by the direct signal contribution with minimal contribution from the reflected signal. As the distance increases, i.e. moving from 5 cm to 170 cm, the reflected contribution signal becomes more dominant, which smears the prompt signal of the direct contribution, enhancing the width of the signal. Hence, the waveform has a smaller amplitude and broader distribution. The fact that the last three signals have a higher peak and are narrower can be explained by the fact that the two components, **"direct"** and **"reflected"**, start to be comparable and arrive at the same time. This causes a superposition of two almost identical signals. In contrast, at closer locations, there was a superposition of two signals with a different delay and shape. Hence the further locations exhibit narrow and higher peaked signals.

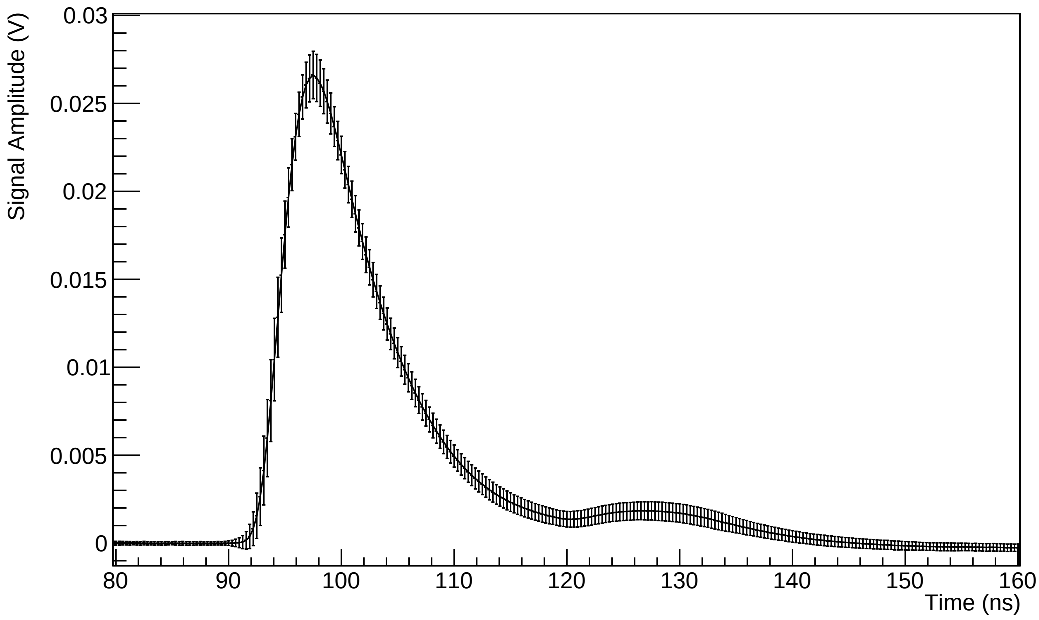

Figure 2.7: Example averaged signal with RMS errors.

Combining the results for both sensors in a single plot will be beneficial for future analysis as it will increase the statistical significance.

Based on the physical understanding described above, the author formulated a relationship for the intensity profile of the signal, which is represented by the integral of the signals. The hypothesis, shown in eq. 2.1 includes two different exponential terms, with the first one representing the direct signal, which solely suffers from absorption, and the second one encompasses the combined effect of the direct and reflected signals.

$$I = I_0(e^{-x/\lambda} + \alpha e^{-(2\cdot 220-x)/\lambda}) \tag{2.1}$$

The fit parameters are the initial intensity, I_0, the effective attenuation length, λ, and the fraction of light which corresponds to the second term, α. The data agree with the functional form of the hypothesis, as shown in fig. 2.9 but return an effective attenuation length of around 160 cm, which is much shorter than expected. This is because our model does not fully describe the complicated geometry of the bar in order to clearly distinguish between competing effects. Thus, we expect the real light path to be around 380cm, accounting for reflections.

As a final check, the full width at half maximum (FWHM) of the averaged signals in fig. 2.8 was calculated and is shown in fig. 2.10. The procedure used to extract the FWHM involved fitting a convolved Gaussian-Landau function to the average signals, which was then used to obtain the FWHM value. The behaviour of the FWHM corroborates the hypothesis proposed above. The FWHM appears to increase and reach a peak at the absolute 170 cm location, which from fig. 2.8 corresponds to the smallest and widest averaged signal. This can be supported by the physical explanation for how light behaves within the bar, which was previously proposed. Around mid-bar, the trigger suffers the most from the superposition of the two components because they have different peaks and are delayed with respect to each other. Thus, the superposition of the two components leads to the widening of the signal, which causes an increase in the FWHM.

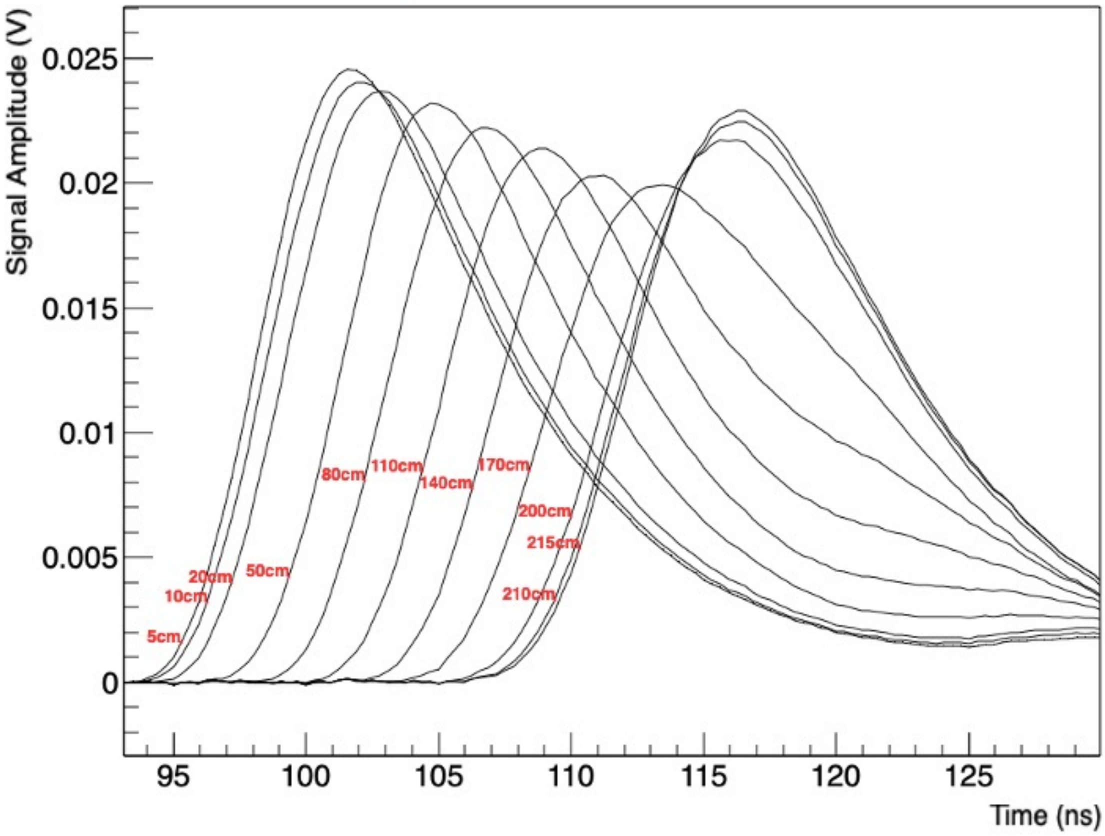

Figure 2.8: Compilation of all averaged signals for one of the two SiPM arrays.

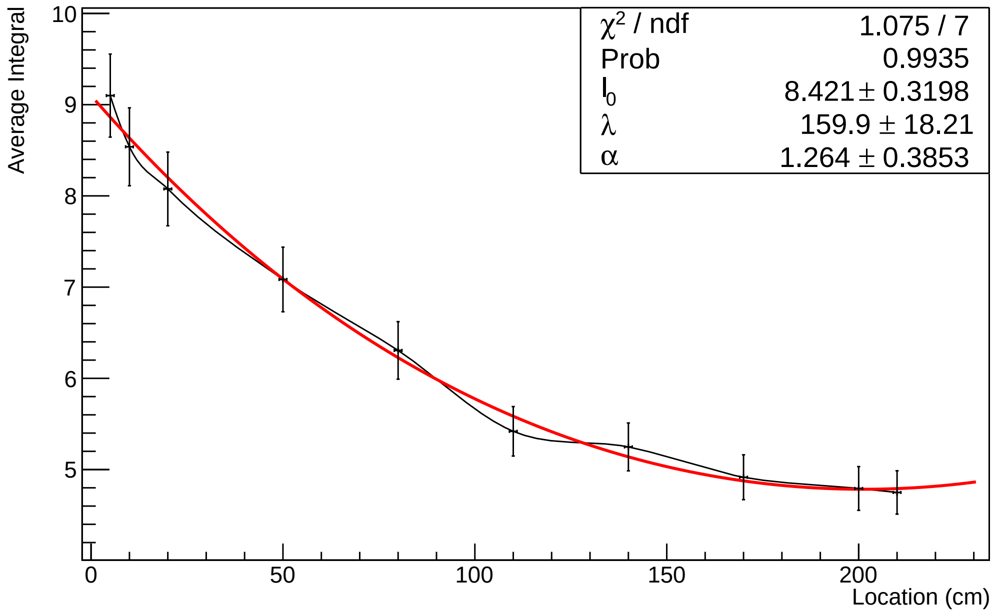

Figure 2.9: Intensity as a function of location fitted with light propagation model.

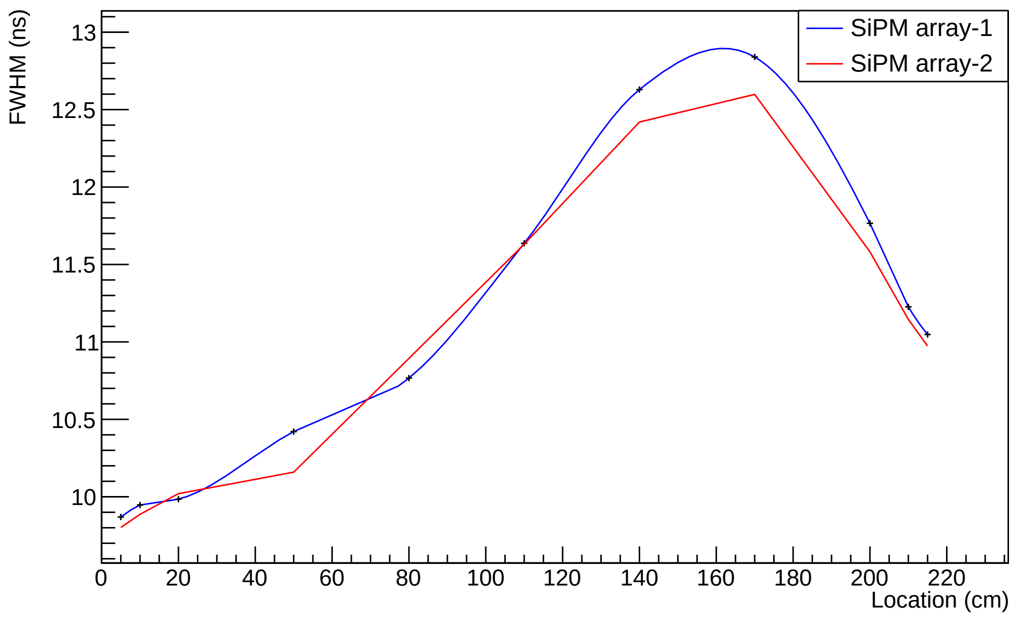

Figure 2.10: FWHM as a function of location for both SiPM arrays.

Chapter 3

Time Resolution of Single-Bar Data

3.1 Time Propagation Distributions

Zero-suppressed time propagation is defined as the time it takes for a signal to propagate from the location of the external trigger to one of the two SiPM arrays at the edges of the bar. This is experimentally calculated by computing the difference between the average time recorded by the four counters of the external trigger and the time recorded by the SiPM array. This time measurement is of utmost importance in characterising the detector's response, determining its time resolution and ultimately the velocity of the signal through the bar. The metric used to define the arrival time of a signal in this investigation is the digital constant fraction discrimination (dCFD) technique whereby the variables t10 and t12 were used with the usual meaning as in 2.2.

For every accepted signal, the value of the zero-suppressed time propagation was calculated. Then, a Gaussian fit was applied to it to extract the mean value of the zero-suppressed time propagation along with its uncertainty. This method of calculating the value of the zero-suppressed time propagation was preferred over using the average signals in fig. 2.8. It was found that fitting the average signals smoothed out the extracted values eliminating the spurious signals arriving out of time. Overall, both methods indicate that the closer the position of the external trigger to the SiPM array under investigation, the lower the values of t10. Moving further away leads to an increase in the time to reach 10% of the peak. This increase can be explained by the fact that the sensor detects more and more light reflected, causing the arrival time of the photons to be more spread, and the signal rises more slowly. Using the light propagation model developed in 2.2, the closest position is dominated by **direct** light leading to a short zero-suppressed time propagation. Conversely, the furthest locations are dominated by **reflected** light causing a shallower rising of the signal, which can explain the change in slope. The positions in the middle experience a balanced combination of both **direct** and **reflected** light and thus exhibit a more linear relationship.

Correcting for the offsets observed in the trigger distributions due to delays caused by cable lengths, fig. 3.1 was produced depicting the zero-suppressed time propagation distributions for both SiPM arrays at the 11 locations. The offset was calculated by fitting a linear function to the first three mean values of the zero-suppressed time propagation distributions and extrapolating to find the y-intercept corresponding to the offset. The offsets were computed for t6, t8, t10 and t12 exhibiting similar behaviour and are shown in Table 3.1. It was assumed that the offset is comprised of two primary components; one constant value corresponding to the length of the cable and a second component related to the percentage of the dCFD used; higher percentage leads to bigger zero-suppressed time propagation. Using the offsets determined, a linear relationship was used to extract the constant offset-common to all- corresponding to the cable length delay. The cable length delay was then used as a correction offset for the time distributions.

3.2 Time Resolution

From fig. 3.1, the width of each zero-suppressed time propagation distribution was extracted utilising the Gaussian fit described in the previous section and used to define the time resolution. The error bars indicate the error associated with each resolution. The results are shown in 3.2

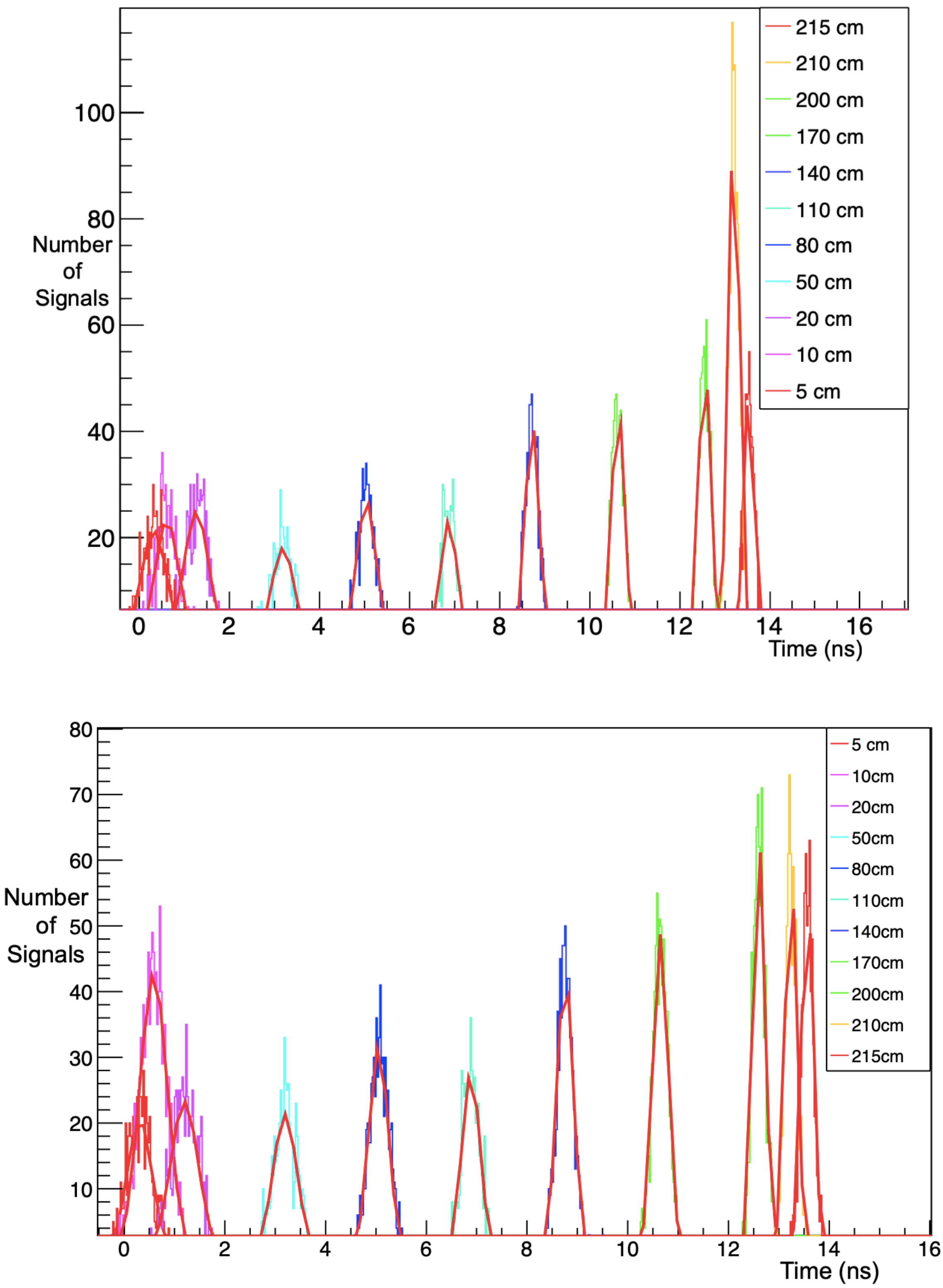

Figure 3.1: zero-suppressed time propagation distribution for SiPM array-1 (top) and SiPM array-2 (bottom) with Gaussian fits.

dCFD metric	SiPM array-1	SiPM array-2
t6	-1.32 ± 0.04	-1.39 ± 0.04
t8	-1.44 ± 0.04	-1.51 ± 0.02
t10	-1.53 ± 0.02	-1.60 ± 0.02
t12	-1.64 ± 0.05	-1.60 ± 0.02

Table 3.1: Table with all the offsets for both SiPM arrays with their errors.

along with the average and weighted average time resolution. The errors can justify the differ-

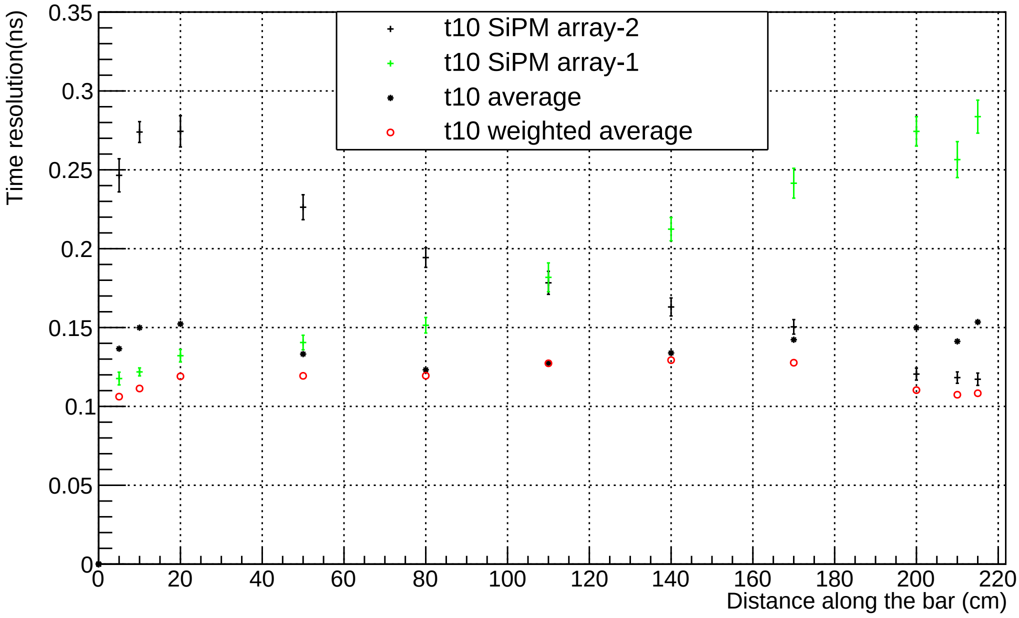

Figure 3.2: Time resolution plots using the t10 dCFD metric.

ence in time resolution for all distances along the bar except the 5 cm location, which shows a different performance when comparing both ends. This could be a possible indication of a small displacement between the two SiPM arrays, which might lead to different results due to the rapidly changing resolution close to the bar ends. The mean time resolution mid-bar is 127 ps for the t10 variable. Repeating the calculation with the t12 variable illustrated that the t10 time resolutions are not consistently bigger/smaller compared to the t12 time resolution which implies that there is no systematic effect incurred by the choice of one variable over the other. Using both variables can provide further advantages in enhancing our understanding of the time resolution plots.

To obtain the best time resolution, indicated by the t10 weighted average graph in fig.3.2, the two end results were combined using the weighted arithmetic mean. This is the optimal way to combine two results with different resolutions. However, we need to reconstruct the precise location of the entry point of the track in the detector. T2K has an excellent tracking performance with a point resolution below 1mm. With this precision, the standard deviation obtained with this method is:

$$\sigma = \sqrt{\frac{1}{\frac{1}{\sigma_1^2} + \frac{1}{\sigma_2^2}}}$$

The combined weighted average σ value is shown also in fig. 3.2. The value varies along the bar length but it shows an excellent performance below 150 ps resolution. The weighted average time resolution computed above does not take into account the error incurred from reconstructing the position in the bar. Therefore it is only valid for near-perfect position reconstruction resolution, giving a weighted mean of 110 ps. Factoring in the tracking position resolution leads to a true resolution that will be in-between the average and weighted average time resolution shown in the figure above.

Chapter 4

Conclusion

The T2K experiment has been commissioned since 2009 to study the properties of neutrino oscillations. It is now due for an upgrade, which involves upgrading the ND280 near detector. As part of the CERN Summer Student Programme, the author has been working on characterising the performance of the ToF detector that will be deployed as part of the upgrade. The focus of the investigation was on single-bar data, with an aim to describe signal delays and report the detector's time resolution by examining the signals recorded at 11 different locations along the bar.

Firstly, the signals were filtered via three cuts to remove saturated, noise and double signals. The saturation cut, which removed signals that exhibited a plateau, removed 5% of the total number of signals removed. Following that, the trigger amplitude signal aimed to discard background noise events removed 90% of all the signal removed, making the second cut the most influential cut performed in the analysis. Lastly, the integral/maximum cut removed the last 5% of all the signals removed and was primarily aimed at eliminating double signals. Once the clean-up was finalised, the remaining signals were used to depict an averaged waveform at each location shown in 2.8. This procedure led to a description regarding light propagation in the single bar, where the significance of each of the two components of light; **"direct"** and **"indirect"**, varied significantly along the bar. At the closest locations, the primary component of the signal was **"direct"** light, leading to a narrow and prominently peaked averaged signal. In contrast, mid-bar, the **"indirect"** component starts becoming more dominant, leading to a smearing of the signal and thus forming a broader and shallower averaged signal. At the end of the bar, both components are comparable and arrive almost simultaneously, thus leading to narrower and higher peaked signals. Using the above interpretation, a model about the intensity of light through the bar was formulated, which agreed well with the data, but led to a much smaller effective attenuation length than expected because the model proposed does not capture the complex geometry of the bar.

Using the accepted signals, the author proceeded to study the distribution of the zero-suppressed time propagation variable. This was done using a dCFD metric to characterise the response of the detector and its time resolution. The mean of the distributions produced for varying locations along the bar agreed with the physical interpretation presented in 2.2. The distributions were then fitted with a Gaussian to extract their width, which represents the time resolution. The time resolution study concluded that all time resolutions but the one at the 5 cm location exhibit comparable performance when comparing both ends of the bar. The difference in the performance of the time resolutions could hint at a small displacement between the SiPM arays. The mean time resolution mid-bar was calculated at 127 ps using t10. The time resolutions were calculated using both t10 and t12. When compared, the t10 time resolutions were not consistently bigger/smaller than the t12 time resolutions, an indication that no systematic bias is incurred when using one or another. In this study, a near-perfect position reconstruction resolution was assumed.

The next steps will involve examining the propagation velocity behaviour in a single bar using the time distributions and time resolution analysis described in this investigation. Afterwards, moving onto the whole panel data and the geometry of the whole TOF detector will allow for a complete track reconstruction which is the final aim of the study of the behaviour of the proposed ToF detector.

Bibliography

[1] Abe, K. et al. (2020) *T2K ND280 Upgrade - Technical Design Report.* [Online] Available from: https://arxiv.org/abs/1901.03750
[2] The T2K Collaboration, n.d. *The T2K Experiment.* [Online] T2k-experiment.org. Available at: https://t2k-experiment.org/t2k/
[3] Uchida Yoshi. ND280 Picture. [Online] Available at: https://www.t2kuk.org/wiki/YoshiUchida/ND280Pictures?action=AttachFile&do=view&target=ND280Exploded-Text-Transparent-Small.png
[4] (2005) *T2K ND280 Conceptual Design Report.*[Online] Available at: http://www.nd280.org/documents/cdr.pdf/view
[5] Eljentechnology.com. n.d. EJ-200, EJ-204, EJ-208, EJ-212 - Plastic Scintillators - Eljen Technology. [Online] Available at: https://eljentechnology.com/products/plastic-scintillators/ej-200-ej-204-ej-208-ej-212